

Experimental and theoretical study of core-excited $3pnd$ Rydberg series of Mg

Matthieu Génévriez , Dominik Wehrli, and Frédéric Merkt*
 Laboratory of Physical Chemistry, ETH Zurich, CH-8093 Zurich, Switzerland

 (Received 7 August 2019; published 26 September 2019)

We present an experimental and theoretical study of the structure and autoionization dynamics of the $(3p_{j_c}nd_j)_{J=1,3}$ core-excited Rydberg states of Mg. Spectra were recorded experimentally for principal quantum numbers n in the range from 30 to 100 using the isolated-core-excitation technique. Large-scale configuration-interaction calculations combined with the exterior-complex-scaling method were also carried out, which do not rely on the assumptions used in the usual R -matrix multichannel-quantum-defect-theory treatment of core-excited Rydberg states. Agreement between theory and experiment is excellent over the entire range of principal quantum numbers studied and allows us to elucidate in detail the structure of the core-excitation spectra. The dominant autoionization mechanisms are identified, and in particular the very fast spin-orbit autoionization of some $(3p_{3/2}nd_j)_J$ states above the $3p_{1/2}$ ionization threshold. We discuss the influence of the principal and total-angular-momentum quantum numbers n and j of the Rydberg electron and the total-angular-momentum quantum number J of the atom on the autoionization dynamics. We also identify previously unobserved resonances attributed to members of the $(3p_{j_c}ng_j)_J$ series.

DOI: [10.1103/PhysRevA.100.032517](https://doi.org/10.1103/PhysRevA.100.032517)

I. INTRODUCTION

Doubly excited states of atoms and molecules are states in which two electrons have been promoted to orbitals not occupied in the ground state. In most cases, they lie energetically above the first ionization threshold and can decay into a more stable, ionic state by spontaneous emission of an electron, a process known as autoionization. This decay results from the Coulomb repulsion between electrons, making the properties of doubly excited states highly sensitive to electron-electron correlations. Doubly excited states have been extensively studied [1–3] since the early experiment of Beutler on doubly excited states of Ar, Kr, and Xe [4].

Core-excited Rydberg states are a class of doubly excited states in which two electrons are asymmetrically excited, one to a high-lying Rydberg state and the other to a low-lying excited state. In the alkaline-earth-metal atoms, core-excited Rydberg states are easily accessible experimentally because these atoms possess only two valence electrons, the remaining electrons forming a closed-shell core which does not significantly influence their properties. Consequently, these elements have received considerable attention from experiment and theory and played an important role in the understanding of autoionizing Rydberg series and the development of multichannel spectroscopy [2]. The low single- and double-ionization potentials of alkaline-earth-metal elements facilitate their study by high-resolution spectroscopy with conventional lasers, especially when compared to the simplest two-electron system, helium, for which synchrotron radiation is required, with comparatively low resolution. From a theoretical perspective, alkaline-earth-metal atoms can be treated as effective two-electron systems, with the advantage that emphasis can be placed on the physical

processes at play in core-excited Rydberg states. Core-excited Rydberg states of alkaline-earth-metal atoms are best described using the jj coupling scheme [2] and will be labeled by $(n_c l_{c_j} n l_j)_J$ hereafter. The quantities n_c , l_c , j_c denote the principal, orbital-angular-momentum, and total-angular-momentum quantum numbers of the inner electron, and n , l , and j are the corresponding quantum numbers of the Rydberg electron. J is the total-angular-momentum quantum number of the atom.

Experimentally, core-excited Rydberg states have been studied in two ways: In photoionization spectra of ground-state atoms recorded following excitation with a single vacuum-ultraviolet photon, they appear as resonances and exhibit typical Beutler-Fano profiles [4,5] resulting from the interference between the direct photoionization and autoionization pathways (see Wehlitz *et al.* [6] for a recent example on Mg). In isolated-core-excitation (ICE) spectra, the atoms are first prepared in a high-lying Rydberg state and, in a second step, photoionization is achieved using a laser with photon energies in the vicinity of a transition of the bare ion [2,7,8]. In the isolated-electron picture, this corresponds to the excitation of the second valence electron to an excited state of the ion core. The direct photoionization of the Rydberg electron in the second step is negligible compared to excitation of the core electron and autoionization. Consequently, ICE spectra exhibit series of Lorentzian-type resonances, indicating the absence of strong Fano-type interferences [9].

Theoretically, a broad range of core-excited Rydberg states of alkaline-earth-metal elements have been studied with remarkable success using the collision-theory framework of multichannel quantum-defect theory (MQDT) [2]. This approach proves particularly powerful when the short-range scattering parameters required by MQDT can be determined *ab initio*, e.g., in eigenchannel R -matrix calculations. The complex structures of numerous alkaline-earth-metal ICE spectra, strongly perturbed by multiple channel interactions,

*merkt@xuv.phys.chem.ethz.ch

were elucidated with this method [2]. An alternative approach, developed in parallel to study core-excited Rydberg states of helium, relies on the direct treatment of the full, two-electron problem by means of a basis-set expansion of the two-electron wave function combined with the complex-scaling method [10–13]. However, this approach was not used to study core-excited Rydberg states of alkaline-earth-metal atoms until the recent work of Fields *et al.* [14], who calculated the quantum defects and autoionization rates of the $(5p_{1/2}np_j)_J$ and $(5p_{1/2}nf_j)_J$ series of Sr.

Magnesium differs from the heavier alkaline-earth-metal atoms (Ca, Sr, Ba) in two ways [15,16]. First, the absence of a $(n_c - 1)d$ excited state of the ion lying between the $n_c s$ ground state and $n_c p$ excited state reduces the number of open channels and the complexity of the problem. Second, the fine-structure splitting of the $3p_{1/2,3/2}$ ionic state is relatively small (91.57 cm^{-1} [17]). Consequently, interactions between the Rydberg series converging to these two thresholds occur over a much broader range of principal quantum numbers of the $np_{3/2}$ series, with n as high as 35, compared to $n = 14$ in Sr and $n = 10$ in Ba. These differences, and the effect they have on ICE dynamics, were investigated in the pioneering works of Dai *et al.* [15] and Schinn *et al.* [16]. They studied ICE spectra for a broad range of $(3p_j nd_j)_J$ core-excited Rydberg states of Mg, with $n = 9\text{--}40$ and $J = 1$ and 3, both experimentally and theoretically within an R -matrix MQDT approach. Their work was later extended by Lindsay *et al.* [18,19], who measured the angular distributions of autoionized electrons, by Lyons *et al.* [20], who studied $(3p_j nf_j)_{J=2,4}$ states, and by Warntjes *et al.* [21], who investigated the influence of strong electric fields on core-excited Rydberg states.

Of particular interest in the context of core-excited Rydberg states is the evolution of the decay dynamics with the quantum numbers n , l , and j describing the Rydberg electron and the total-angular-momentum quantum number J . For example, increasing n or l reduces the strength of electron-electron interactions and progressively uncouples the Rydberg electron from the ionic core [22]. This behavior offers attractive prospects in the field of quantum optics and quantum simulation with alkaline-earth-metal elements [23–25]. Provided that the autoionization rate is small, the core-excitation transition may be used to manipulate Rydberg atoms with light while the long-range potential associated with the large dipole moment of the Rydberg electron allows the study of interactions between Rydberg atoms and the simulation of many-body quantum dynamics [23]. The fluorescence of core-excited Rydberg atoms has already been used to image ultracold neutral plasmas [26–28]. Whereas the effects of n and l on the coupling between the Rydberg electron and the ionic core are extensively documented [22], information on the effects of j and J is much scarcer. This work aims at filling this gap.

We present an experimental and theoretical study of the $(3p_j nd_j)_J$ ($J = 1, 3$) core-excited Rydberg states of Mg. Our experiment, presented in Sec. II, is based on the ICE technique. We recorded core-excitation spectra from $3snd \ ^1D_2$ Rydberg states for principal quantum numbers in the range from $n = 31$ to 80. The high n values and the high spectral resolution reached in our study enabled the observation of spectral structures that had not been observed previously. The theoret-

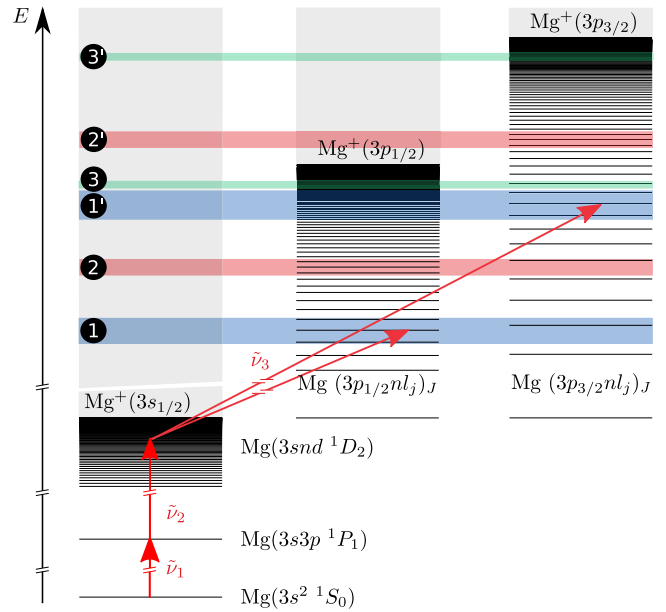


FIG. 1. Schematic diagram (not to scale) of the energy-level structure and excitation scheme used to study the core-excited $(3p_j nd_j)_J$ states of Mg. The shaded blue, red, and green regions, along with the corresponding labels on the left-hand side, indicate the ranges of energies probed experimentally, in which the series interact.

ical approach, detailed in Sec. III, is based on a large-scale configuration-interaction (CI) calculation combined with the exterior-complex-scaling (ECS) technique. The comparison of the calculated and experimental high-resolution spectra, presented in Sec. IV, provides a stringent test for the theory and illustrates the high accuracy and capability of the CI-ECS approach. Particular attention is paid to the description of the dynamics of the core-excited Rydberg states in dependence of the principal quantum number n and of the fine-structure quantum numbers j and J .

II. EXPERIMENTAL SETUP

The experiment relies on the resonant multiphoton excitation of $\text{Mg}(3s^2 \ ^1S_0)$ ground-state atoms to $(3p_j nd_j)_J$ core-excited Rydberg states following the ICE scheme depicted in Fig. 1. In a first step, two pulsed dye lasers are used to excite the atoms from the ground state to $3sns \ ^1S_0$ and $3snd \ ^1D_2$ Rydberg states by $(1 + 1')$ resonance-enhanced multiphoton excitation via the $3s3p \ ^1P_1$ state. The values of the quantum defects of these series are 1.525234(29) and 0.61197(3), respectively [29]. Under our experimental conditions, the neighboring $3s(n+1)s$ and $3snd$ pairs of Rydberg states can be resolved up to $n \simeq 60$. Below this value, $3snd$ states can thus be selectively populated by choosing the corresponding excitation frequency. The square of the transition dipole matrix element from the $3s3p \ ^1P_1$ state to the $3sns \ ^1S_0$ state is about 200 times smaller than that to $3snd \ ^1D_2$ states. Consequently, the excitation probability to the s Rydberg series is much smaller than that to the d Rydberg series. When recording the photoexcitation spectrum of the $3s3p \ ^1P_1$ state to Rydberg states with $n = 40\text{--}60$, we did not observe lines corresponding

to $3sns\ ^1S_0$ states. We thus neglect the contribution of $3sns$ Rydberg states to the spectra presented in this article.

In the independent-electron approximation, the second excitation step corresponds to the excitation of the $3s_{1/2}$ core electron to the $3p_{1/2}$ or $3p_{3/2}$ excited states, and is achieved using a third pulsed dye laser. To ensure that the excitation occurs in a sequential manner, the pulses of the third laser are delayed with respect to the pulses of the first and second lasers by $\simeq 4$ ns, a value corresponding to their respective full widths at half-maximum. Core-excitation spectra are recorded by scanning the wave number $\tilde{\nu}_3$ of the third dye laser in the vicinity of the $3s - 3p_{1/2}$ and $3s - 3p_{3/2}$ isolated-core transitions, with wave numbers of $35\,669.31\text{ cm}^{-1}$ and $35\,760.88\text{ cm}^{-1}$, respectively [17], and monitoring the Mg^+ ion yield. The wave numbers $\tilde{\nu}_1$ and $\tilde{\nu}_2$ of the first and second lasers are kept fixed at the position of the selected $3snd\ ^1D_2$ Rydberg state (see Fig. 1).

The experimental setup has been described in detail previously [30,31]. Briefly, magnesium atoms are formed by laser ablation of a Mg rod by the second harmonic of a pulsed Nd:YAG laser inside the nozzle of a pulsed-supersonic-expansion source. They are entrained and cooled by the N_2 carrier gas released by the pulsed valve. The atomic beam is collimated 8 cm downstream from the nozzle by a 4-mm-diameter skimmer before it enters the photoionization chamber. In the photoionization chamber, the atomic beam is intersected at right angles by the light pulses from three commercial, frequency-doubled dye lasers pumped by the second harmonic of a seeded Nd:YAG laser. Their wave numbers, denoted $\tilde{\nu}_1$, $\tilde{\nu}_2$, and $\tilde{\nu}_3$ below, are measured with a commercial wavemeter with a specified absolute accuracy of 0.02 cm^{-1} . All three lasers are linearly polarized along the same direction, perpendicular to that of the atomic beam. The wave number of the first laser is set to $35\,051.26\text{ cm}^{-1}$, corresponding to the $3s^2\ ^1S_0 - 3s3p\ ^1P_1$ transition. Its pulse energy is attenuated to about $50\ \mu\text{J}$ in order to prevent direct ionization of atoms in the $3s3p\ ^1P_1$ excited state. The pulse energy of the second laser is $\simeq 1\text{ mJ}$ and its bandwidth estimated to be 0.15 cm^{-1} from the full widths at half-maximum of the lines in the pulsed field ionization spectrum of the Rydberg $3snd\ ^1D_2$ series. From previous work [30], we estimate the bandwidth of the frequency-doubled output of the third laser to be of the order of 0.1 cm^{-1} . Its pulse energy is attenuated to below $25\ \mu\text{J}$ in order to avoid power and saturation broadening.

The interaction between the atoms and the laser pulses occurs inside a 5.8-cm-long stack of five cylindrical, equally spaced, and resistively coupled electrodes. The stack is surrounded by two concentric mu-metal shields to suppress stray magnetic fields. 600 ns after the laser pulses, an electric-field pulse of about 120 V/cm is applied to the electrode stack to accelerate the positive ions into a linear time-of-flight (TOF) region, at the end of which they are detected using a microchannel-plate (MCP) detector. The MCP signal is amplified and measured on a fast digital oscilloscope, itself connected to a computer for data acquisition and analysis. We record, in the TOF trace, the signals corresponding to the $^{24}\text{Mg}^+$, $^{25}\text{Mg}^+$, and $^{26}\text{Mg}^+$ ions separately. All results presented below are for $^{24}\text{Mg}^+$. For principal quantum numbers n of the Rydberg electron above $\simeq 50$, the electric field generated by the extraction pulse is sufficient to field ionize

the Rydberg atoms. In order to distinguish between photoions and ions produced by pulsed-field ionization (PFI) of Rydberg states, we follow the procedure described in Ref. [31], and apply a $2.2\text{-}\mu\text{s}$ -long electric field of 1.4 V/cm to the electrode stack, 300 ns after the laser interaction but prior to the large extraction pulse. This separates the photoionization signal from the PFI signal in the TOF trace and allows their recording in distinct spectra.

Several effects influence the intensity distributions of the measured spectra. First, fluctuations of the number of Mg atoms in the beam, caused by inherent instabilities in the laser-ablation process, can affect the signal strengths. Fast fluctuations are eliminated by recording the signal amplitude at a given wave number for 125 experimental cycles and subsequently averaging the data. Long-term fluctuations, on the order of several minutes to hours, are not corrected for. To ensure the consistency of the relative intensities of the spectra in the $3p_{1/2}$ and $3p_{3/2}$ regions, we carried out fast, low-resolution scans of each region, which we used to normalize the intensities measured in the slow, high-resolution scans. The spectra were also corrected for variations of the pulse energy of the third laser. Residual saturation and power broadening, albeit minimized, can alter slightly the shape of the spectra.

Photoionization spectra have been recorded for three different ranges of principal quantum numbers n of the Rydberg electron, labeled 1, 2, 3 and 1', 2', 3' in Fig. 1, and corresponding to the excitation of the inner electron to the $3p_{1/2}$ and $3p_{3/2}$ states, respectively. In regions 1 and 1', around $n = 31$, the binding energy ΔE_n of the nd Rydberg electron is slightly larger than the $3p_{1/2} - 3p_{3/2}$ fine-structure splitting of the ion (91.57 cm^{-1} [17]). In this case, the core-excited Rydberg states populated by ICE typically have energies below the $3p_{1/2}$ threshold [see Eq. (9)] and can only decay into the continua associated with the $3s_{1/2}$ ion core. In regions 2 and 2', around $n = 39$, ΔE_n is slightly smaller than the ionic fine-structure splitting. The continua associated with the $3p_{1/2}$ ion core are therefore energetically accessible to $(3p_{3/2}nd_j)_I$ states and must be considered (see region 2' in Fig. 1). In regions 3 and 3', with n in the range from 60 to 80, the open channels are the same as in the second regions, but the decay dynamics are slower because of the reduced interaction between the core and highly excited Rydberg electrons.

III. THEORY

The theoretical description of high- n , core-excited Rydberg states is challenging because the total electronic wave function extends very far away from the nucleus and, at the same time, properties such as quantum defects and autoionization rates critically depend on the detailed behavior of the wave function close to the nucleus. In the R -matrix MQDT approach generally used to study core-excited Rydberg states, these apparently contradicting requirements are met by partitioning the configuration space into inner ($r < R_0$) and outer ($r \geq R_0$) regions [2]. The wave function associated with the N -electron ion core is confined within the inner region, where the full $(N + 1)$ -electron problem must be solved. In contrast, only the Rydberg electron is present in the outer region, where its interaction with the ion core is assumed to be

purely Coulombic, i.e., correlations with the core electrons are neglected. The connection between the inner and outer regions is expressed in terms of the R matrix used in scattering theory [32], which can be calculated *ab initio*. Physical quantities such as the Rydberg density of states can be derived from the R matrix, or equivalently from the reaction matrix K , using MQDT [33]. They are described as the result of the scattering of the Rydberg electron off the ion core. To reduce the complexity of the problem, some channels can be neglected, such as the $(3p_{j_c}ng_{j_c})_I$ channels in Mg [15,16]. A channel is specified by the state of the ionic core (e.g., $3p_{j_c}$), the set of appropriate angular-momentum quantum numbers of the Rydberg electron (e.g., l and j) and the set of angular-momentum quantum numbers of the atomic system (e.g., J).

An alternative approach, used extensively to study the doubly excited states of helium [10–13] and more recently Sr [14], consists in solving the full two-electron problem over the entire space spanned by the total wave function. The approximations inherent to the R -matrix MQDT approach are avoided in this way and the bielectronic interaction is treated everywhere to all orders. Continuum states and resonances can be accounted for using the complex-scaling method [34,35]. The two-electron wave function is expanded in a large basis set used to construct the two-electron Hamiltonian. Diagonalization of the large, complex-rotated Hamiltonian matrix yields, in a straightforward manner, the energies and associated complex-rotated wave functions of both bound states and autoionizing resonances, along with the widths of the latter. All channels are automatically included in the calculation. Another strength of this approach is that the photoionization cross section from any initial Rydberg state can be calculated directly and in an absolute manner, without resorting to the approximations commonly used in the R -matrix MQDT treatment of ICE and, in particular, without neglecting the direct photoionization of the Rydberg electron. R -matrix MQDT, however, offers the advantage that it enables the description of the coupled Rydberg series, including autoionization, in a single configuration-interaction calculation carried out at short range [2].

In the following, we describe a configuration-interaction-type approach within the two-active-electron approximation, where the total wave function is expanded in terms of one-electron wave functions of the Mg^+ ion calculated on a grid. We require this method to be simultaneously accurate, in order to allow comparison with the experimental spectra recorded with a resolution of 0.1 cm^{-1} , and computationally tractable even for Rydberg states as high as $n = 80$. To significantly reduce the numerical complexity, we exploit the inherent asymmetry of the problem, i.e., the fact that one electron remains close to the Mg^{2+} core while the other extends far away from it. A similar approach was used by Fields *et al.* [14] to calculate the autoionization rates of high-lying core-excited Rydberg states of the Sr atom.

A. Atomic structure

As in previous works [2,36], we consider explicitly only the two valence electrons of Mg. The remaining 10 electrons of the $\text{Mg}^{2+}(1s^22s^22p^6)$ closed-shell core are accounted for through an empirical model potential. In the following, atomic

units are used unless stated otherwise. The electronic Hamiltonian in the two-active-electron approximation is

$$H = -\frac{\nabla_1^2}{2} - \frac{\nabla_2^2}{2} + V_{l_1}(r_1) + V_{l_2}(r_2) + V_{s_1l_1j_1}^{\text{SO}}(r_1) + V_{s_2l_2j_2}^{\text{SO}}(r_2) + \frac{1}{r_{12}}, \quad (1)$$

where r_1 and r_2 are the radial coordinates of the two electrons described by the quantum numbers (l_1, s_1, j_1) and (l_2, s_2, j_2) respectively. r_{12} is the distance between the two electrons. V_l denotes the l -dependent model potential describing the Mg^{2+} core and V_{slj}^{SO} is the spin-orbit interaction. We use the model potential

$$V_l(r) = -\frac{1}{r} \left[2 + (Z-2)e^{-\alpha_1 r} + \alpha_2^l e^{-\alpha_3^l r} \right] - \frac{\alpha_{\text{cp}}}{2r^4} \left[1 - e^{-(r/r_c)^6} \right] \quad (2)$$

introduced by Luc-Koenig *et al.* [36], who optimized the parameters α_1^l , α_2^l , α_3^l , and r_c to reproduce as closely as possible the experimental energies of the Mg^+ ion. α_{cp} is the dipole polarizability volume of the Mg^{2+} core, $0.49 a_0^3$, determined experimentally by Bockasten [37]. The spin-orbit interaction is given by [2,38]

$$V_{slj}^{\text{SO}}(r) = \frac{\alpha^2}{2} \vec{l} \cdot \vec{s} \frac{1}{r} \frac{dV_l}{dr} \left[1 - \frac{\alpha^2}{2} V_l(r) \right]^{-2}, \quad (3)$$

where α is the fine-structure constant. For the model potential given in Eq. (2), the spin-orbit interaction calculated with Eq. (3) yields a fine-structure splitting of the $3p_{1/2}$ and $3p_{3/2}$ levels of Mg^+ overestimated by 14 cm^{-1} compared to the experimental value (91.57 cm^{-1} [17]). However, the overall quality of the present calculation critically depends on the accuracy of the threshold energies, and in particular on the relative positions of the $3p_{1/2}$ and $3p_{3/2}$ thresholds. We have therefore scaled the spin-orbit interaction for all values of l and j by a factor of 0.7875 in order to reproduce the correct threshold energies.

The two-electron wave function is expanded in a basis of antisymmetrized products of two single-electron wave functions,

$$\psi_{JM}(\mathbf{r}_1, \mathbf{r}_2) = \sum_{n_1, l_1, j_1} \sum_{n_2, l_2, j_2} C_{n_1 l_1 j_1 n_2 l_2 j_2}^J \times \mathcal{A} \left[\frac{u_{n_1 l_1 j_1}(r_1)}{r_1} \frac{u_{n_2 l_2 j_2}(r_2)}{r_2} \Lambda_{l_1 j_1 l_2 j_2}^{JM}(\hat{\mathbf{r}}_1, \hat{\mathbf{r}}_2) \right], \quad (4)$$

where $C_{n_1 l_1 j_1 n_2 l_2 j_2}^J$ are expansion coefficients and \mathcal{A} is the antisymmetrization operator. The radial parts of the one-electron wave functions are denoted by $u_{nlj}(r)/r$. The angular and spin parts of any two-electron basis vector are represented by $\Lambda_{l_1 j_1 l_2 j_2}^{JM}(\hat{\mathbf{r}}_1, \hat{\mathbf{r}}_2)$ and are built from one-electron spherical harmonics and spinors using standard angular-momentum algebra [39]. $\hat{\mathbf{r}}_1$ and $\hat{\mathbf{r}}_2$ are the unit vectors associated with the positions of both electrons. As explained by Aymar *et al.* [2], the jj -coupling scheme must be used to describe core-excited Rydberg states of alkaline-earth-metal atoms. The expansion

coefficients C contain the normalization constants of the two-electron basis vectors.

One-electron basis functions in the above configuration-interaction expansion are chosen to be the one-electron orbitals of Mg^+ . The reduced radial one-electron wave functions $u_{nlj}(r)$ are thus solutions of the one-electron radial equation

$$\left(-\frac{1}{2} \frac{d^2}{dr^2} + \frac{l(l+1)}{2r^2} + V_l(r) + V_{slj}^{\text{SO}}(r) - \epsilon_{nlj} \right) u_{nlj}(r) = 0. \quad (5)$$

The solutions $[\epsilon_{nlj}, u_{nlj}(r)]$ of the above equation are determined numerically with the finite-element discrete-variable-representation (FEM-DVR) method (see, e.g., Rescigno and McCurdy [40] and Scrinzi and Elander [41]).

In the FEM-DVR method, Eq. (5) is solved on a nonuniform grid subject to the condition that eigenfunctions vanish at both end points. The physical r space is truncated to a finite size $[0, r_{\text{max}}]$ and further partitioned into several, nonoverlapping but contiguous elements. Equation (5) is solved in each element using a DVR method with the boundary condition that eigenfunctions must be continuous across adjacent elements. We use the DVR method of Manolopoulos and Wyatt based on the Gauss-Lobatto quadrature [42] (see also Rescigno and McCurdy [40]). With this procedure, the end points of the global grid ($r = 0, r_{\text{max}}$) are explicitly included in the calculation and the behavior of the wave function at the singularity of the Coulomb potential ($r = 0$) is correctly accounted for. The method requires the physical space spanned by a given element to be mapped onto the $[-1, 1]$ space of the Legendre polynomials underlying the Gauss-Lobatto quadrature. We use for that purpose the linear algebraic mapping proposed in [40]. As in all DVR methods, for a number N of grid points, the radial Schrödinger equation (5) is reduced to a $(N-2) \times (N-2)$ -matrix form, the diagonalization of which yields $N-2$ eigenenergies and eigenvectors. The eigenvectors are proportional to the values of the wave functions at the grid points. Subsequent calculations of matrix elements involving these eigenvectors can be carried out using the same Gauss-Lobatto quadrature without loss of accuracy.

The FEM-DVR approach possesses excellent convergence properties with respect to the grid size, and accurate energies can be calculated by evaluating the wave functions at only a small number of grid points, even for high Rydberg states. This allows a compact representation of the two-electron basis vectors and significantly reduces the computational cost of evaluating matrix elements of the two-electron Hamiltonian. Moreover, the finite-element character of the approach provides flexibility in the definition of the grid. In particular, we define an element with a dense grid close to the nucleus (r small) and another element, spanning the rest of configuration space, with a sparser grid. We thus ensure that the bielectronic repulsion, which is large in the core region, can be accurately calculated while keeping the grid size small. This feature is particularly relevant when treating the high-lying Rydberg states considered in this work.

In the present calculations, we use two elements spanning the ranges $[0, 100] a_0$ and $[100, 17600] a_0$ and containing 101 and 551 grid points, respectively. For given values of l and j of the electron, 649 basis functions are calculated. The lowest

ones represent bound Rydberg states of Mg^+ with $n \lesssim 90$ and we verified that their energies are converged to better than 10^{-13} hartree. Above $n \simeq 90$, the radial extent of the Rydberg wave function becomes comparable to and eventually larger than the size of the truncated r space. Therefore, the remaining solutions represent positive-energy states in a finite box and provide a discretized version of the continuum (see, e.g., Persson *et al.* [43]). After scaling the spin-orbit operator by the factor of 0.7875, as discussed above, the energies of the low-lying states of Mg^+ are reproduced to within less than 1 cm^{-1} of the measured values [17] in most cases. In particular, the ionization energy of the $3s_{1/2}$ state is smaller by 0.16 cm^{-1} than the reference value [17], while those of the $3p_{1/2}$ and $3p_{3/2}$ are smaller by about 0.2 cm^{-1} .

The computation of the matrix elements associated with the one-electron operators in the two-electron Hamiltonian given by Eq. (1) is straightforward because basis vectors are built from products of one-electron spin orbitals. The calculation of two-electron matrix elements associated with the bielectronic repulsion operator $1/r_{12}$ is more difficult. We start from its multipole expansion

$$\frac{1}{r_{12}} = \sum_q \frac{4\pi}{2q+1} \frac{r_{<}^q}{r_{>}^{q+1}} \sum_{m=-q}^q Y_{qm}^*(\hat{\mathbf{r}}_{<}) Y_{qm}(\hat{\mathbf{r}}_{>}), \quad (6)$$

with $r_{<} = \min(r_1, r_2)$ and $r_{>} = \max(r_1, r_2)$. $Y_{qm}(\hat{\mathbf{r}})$ denote spherical harmonics. The matrix elements associated with $1/r_{12}$ can be separated into radial and angular integrals. Angular integrals can be calculated analytically using standard angular-momentum algebra [39,44]. The radial, Slater integral associated with the q th term of the above expansion can be written, in a general form, as [39]

$$\begin{aligned} & \iint dr_1 dr_2 u_{\alpha'}(r_1) u_{\beta'}(r_2) \frac{r_{<}^q}{r_{>}^{q+1}} u_{\beta}(r_2) u_{\alpha}(r_1) \\ &= \int_0^{r_{\text{max}}} dr_1 u_{\alpha'}(r_1) u_{\alpha}(r_1) \left[\int_0^{r_1} dr_2 u_{\beta'}(r_2) \frac{r_2^q}{r_1^{q+1}} u_{\beta}(r_2) \right. \\ & \quad \left. + \int_{r_1}^{r_{\text{max}}} dr_2 u_{\beta'}(r_2) \frac{r_1^q}{r_2^{q+1}} u_{\beta}(r_2) \right], \quad (7) \end{aligned}$$

where α and β denote the quantum numbers n, l , and j of the first and second electrons, respectively. Unfortunately, the integrals over r_2 cannot be evaluated directly with Gauss-Lobatto quadrature [45,46]. To overcome this problem, we follow the method of McCurdy *et al.* [46] and reexpress the integrals over r_2 in Eq. (7) as solutions of a Poisson differential equation. This equation can be solved by another application of the FEM-DVR method, with the same high-accuracy properties. Once the integrals over r_2 are calculated, the integration over r_1 can be straightforwardly carried out to obtain the bielectronic repulsion matrix elements.

In the FEM-DVR method outlined above, wave functions are required to vanish at the end points of the grid and are consequently square integrable. By essence, the method is not suited for treating processes involving continuum electrons, such as photoionization or autoionization. To overcome this limitation, we use the exterior-complex-scaling (ECS) method [47], which was already applied to atomic systems by, e.g., McCurdy *et al.* [46]. The ECS method relies on the fact

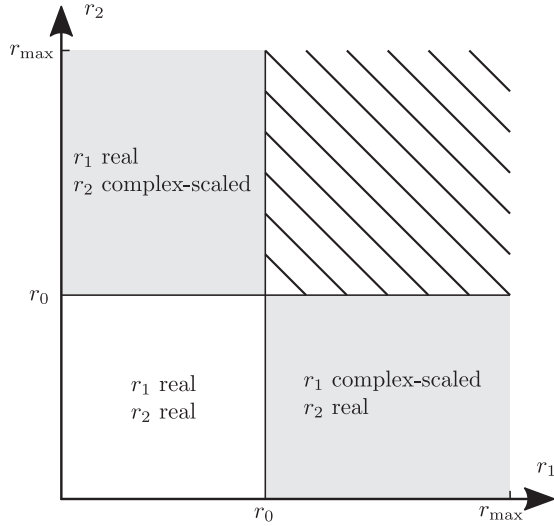


FIG. 2. Schematic representation of the two-electron radial configuration space used in the ECS method. In the hatched region, both electrons are far away from the nucleus and both coordinates are complex scaled. For the problem considered, the amplitude of the two-electron wave function in this region is exponentially small.

that, upon rotation of the radial coordinate into the complex plane, outgoing waves decay exponentially as $r \rightarrow \infty$ and can thus be represented exactly by any complete set of square-integrable functions [35]. Consequently, one can treat autoionizing, core-excited Rydberg states with the CI expansion of Eq. (4) and a basis of two-electron functions built from square-integrable one-electron orbitals calculated with the FEM-DVR method. In practice, ECS amounts to rotating, by an angle $\theta > 0$, the radial coordinates r_1 and r_2 of the two electrons into the complex plane beyond a certain radius r_0 ,

$$r \rightarrow \begin{cases} r & \text{if } r < r_0, \\ r_0 + (r - r_0)e^{i\theta} & \text{if } r \geq r_0, \end{cases} \quad (8)$$

as schematically depicted in Fig. 2. The calculation of both one-electron basis functions with the FEM-DVR method and the two-electron Hamiltonian must be carried out along the contour defined by the complex-rotated r values, resulting in complex-valued wave functions and eigenenergies.

The advantage of ECS over uniform complex scaling, where the r coordinates are complex rotated in the entire configuration space ($r_0 = 0$) [35], stems from the fact that we consider only the single ionization of states in which the two electrons are spatially well separated. By setting the ECS radius r_0 larger than the region of r spanned by the inner electron, only the outer electron evolves in the complex-scaled region, while dynamics of the ionic core are described by usual, real-valued r coordinates (see Fig. 2). Complex scaling requires the use of L^2 complete or nearly complete basis sets [48]. The use of ECS allows one to remove this requirement for the inner electron, which can be described by a small set of core orbitals that possess negligible amplitudes in the outer region. ECS thus greatly reduces the size of the CI expansion in Eq. (4). By limiting the description of the inner electron to core orbitals, we implicitly neglect the two-electron dynamics

in the region depicted by the hatched area in Fig. 2, where both radial coordinates are large. This assumption is clearly valid for core-excited Rydberg states. ECS introduces a discontinuity in the derivative of the wave function at r_0 , which can be accounted for exactly using, for example, the FEM-DVR method outlined above [46].

The complex-rotated, two-electron Hamiltonian matrix $H(\theta)$ is non-Hermitian, complex symmetric, and has eigenvalues given by $E_i - i\Gamma_i/2$, where E_i and Γ_i are the energies and widths of the eigenstates. These eigenvalues can be classified into three groups: (i) those independent of both the complex-rotation angle θ and the basis-set size N , and having $\Gamma_i = 0$. They correspond to bound states with energies E_i ; (ii) those also independent of θ and N but with $\Gamma_i > 0$. They correspond to resonances with energies E_i and widths Γ_i ; (iii) those depending on θ . They belong to extended quasidiscretized continua that are associated with continuum states of the electron, and their eigenenergies are rotated by approximately -2θ with respect to the real axis [34]. The independence of the eigenenergies of resonance states with respect to θ , N and the ECS radius r_0 must be ensured by systematically increasing the size of the truncated, square-integrable basis set until convergence is reached.

The calculations presented in Sec. IV are carried out with complex rotation by an angle $\theta = 5^\circ$ applied to the second element of the FEM-DVR calculation ($r_0 = 100 a_0$). For a total angular momentum $J = 3$, the two-electron wave function is expanded in a basis of 32 928 vectors corresponding to all configurations obtained from the $3s_{1/2}$, $3p_{1/2}$, $3p_{3/2}$, $3d_{3/2}$, $3d_{5/2}$, $4s_{1/2}$, $4p_{1/2}$, and $4p_{3/2}$ orbitals describing the inner electron and a large set of orbitals representing the outer electron [649 orbitals per (l, j) channels]. For $J = 1$, this number reduces to 25 841 because of the reduced number of channels. We checked that the energies and widths of $(3s_{1/2}nl_j)_J$ Rydberg states and $(3p_{j_c}nl_j)_J$ core-excited Rydberg states are converged to better than 0.03 cm^{-1} , a value smaller than the present experimental resolution. Therefore, the small differences between theory and experiment can be attributed to the imperfection of the model potential and the neglect of dynamical interactions between the valence electrons and the Mg^{2+} core.

To assess the overall accuracy of the calculations, one can compare the computed energies of the bound Rydberg series of Mg to available data. To this end, we determined the quantum defects of the calculated $3snl$ series by fitting the energies of all states in the range $n = 10\text{--}80$ with Rydberg's formula

$$E_{nl} = E_{\text{Mg}^+(3s)} - \frac{R_{\text{Mg}}^{24}hc}{(n - \delta_l)^2}, \quad (9)$$

where $E_{\text{Mg}^+(3s)}$ is the energy associated with the first ionization threshold and R_{Mg}^{24} is the mass-corrected Rydberg constant. The computed quantum defects of all singlet series $3snl$ with $l = 0\text{--}4$ lie within ± 0.008 of the highly accurate experimental values of MacAdam *et al.* [29]. Those of triplet Rydberg series are within ± 0.01 of the values determined by Amemiya *et al.* [49]. We further assessed the accuracy of the calculations by comparing the energies and widths of members of the core-excited $(3p_{j_c}nd_j)_3$ and $(3p_{j_c}nf_j)_{J=2,4}$ Rydberg series to those reported by Dai *et al.* [15] and

Lyons *et al.* [20]. Quantum defects associated with the present theoretical results agree within ± 0.02 with quantum defects derived from previous experimental data, with the exception of a few states for which, however, the quantum defects do not differ by more than ± 0.07 [50]. The calculated widths agree within error bars (1σ) with the experimental widths reported by Lyons *et al.* [20] in most cases, and within 2σ in all cases. Overall, there is excellent agreement between the present calculations and available experimental data. We thus conclude that the method discussed above for calculating the properties of core-excited Rydberg states is both reliable and accurate.

B. Photoionization cross section

In the experiment, the measured signal is related to the photoionization cross section σ of $3snd\ ^1D_2$ states for photon energies in the vicinity of the $3s_{1/2} - 3p_{1/2}$ and $3s_{1/2} - 3p_{3/2}$ core transitions of the Mg^+ ion. This cross section can be calculated from the wave functions obtained by diagonalization of the two-electron Hamiltonian for the relevant total angular momenta J and J' relative to the initial and final states. We follow Rescigno and McKoy [51] and write σ as

$$\sigma(\omega) = \frac{4\pi\omega}{c} \sum_{J',M'} \begin{pmatrix} J=2 & 1 & J' \\ M & q & -M' \end{pmatrix}^2 \times \text{Im} \sum_i \frac{\langle \bar{\psi}_{i,\theta,J'} | \boldsymbol{\mu}^{(1)}(r_\theta) | \psi_{3snd,J=2} \rangle^2}{E_{i,\theta,J'} - E_{3snd} - \omega}, \quad (10)$$

where ω is the angular frequency of the radiation and c stands for the speed of light. The initial state $|\psi_{3snd,J=2}\rangle$ and final state $|\psi_{i,\theta,J'}\rangle$ have energies E_{3snd} and $E_{i,\theta,J'}$ and magnetic quantum numbers M and M' , respectively. The parameter q indicates the ellipticity of the light polarization, with $q = 0$ in the case of linear polarization. The quantity $\langle \bar{\psi}_{i,\theta,J'} | \boldsymbol{\mu}^{(1)} | \psi_{3snd,J=2} \rangle$ is the reduced matrix element of the complex-rotated transition-dipole operator, expressed in the length gauge in this work. $\langle \bar{\psi} |$ denotes the complex conjugate of $\langle \psi |$, i.e., the transpose of $|\psi\rangle$ [48]. The sum over i in Eq. (10) runs over all final states with given J' and M' quantum numbers.

In writing Eq. (10), we assumed that the initial $3snd\ ^1D_2$ Rydberg states are prepared with $J = 2$ and M fixed. Moreover, since they are excited from the $3s^2\ ^1S_0$ state by two linearly polarized lasers with parallel polarizations, dipole selection rules impose that $M = 0$. Core excitation is realized by a third laser with a linear polarization ($q = 0$) parallel to those of the other two, implying $M' = 0$. Under these conditions, Eq. (10) predicts that dipole excitation is allowed only to final states with $J' = 1$ and 3 . However, weak features in the experimental spectra can be unambiguously assigned to $J' = 2$ resonances. This apparent deviation from expectations may be explained by (i) the imperfect polarization of the laser light; (ii) a slight angle between the polarization of the Rydberg-excitation and core-excitation lasers; (iii) depolarization of the Rydberg atoms during the interval between the Rydberg-excitation and core-excitation laser pulses caused by nonuniform stray electric fields. These effects would induce either a distribution of q values or a distribution of M values

for the $3snd$ Rydberg state. Since the extent to which these effects occur is unknown, we have empirically added to the total cross section a small $J' = 2$ component. The best match to the experimental spectra was obtained when replacing the square of the Wigner $3j$ symbol for the $J' = 2$ term in the sum of Eq. (10) by 0.01 . This correction is small compared to the square of the Wigner $3j$ symbols for $J' = 1$ and 3 , which are equal to $\frac{2}{15}$ and $\frac{3}{35}$, respectively.

For the direct comparison between theory and experiment, the theoretical cross section was convoluted with a Gaussian with a full width at half-maximum of 0.1 cm^{-1} corresponding to the laser bandwidth. To account for a weak saturation of the excitation, theoretical core-excitation spectra were calculated from the convoluted cross section $\sigma^c(\omega)$ using

$$S_{\text{th}} = 1 - \exp[-\sigma^c(\omega)I_0\Delta t/(\hbar\omega)], \quad (11)$$

where I_0 represents the average laser intensity in the interaction volume.

IV. RESULTS

A. Experimental results and qualitative analysis with the ICE model

The experimental $3s_{1/2} - 3p_{1/2}$ and $3s_{1/2} - 3p_{3/2}$ core-excitation spectra from the $3s31d$, $3s39d$, $3s60d$, and $3s80d\ ^1D_2$ Rydberg states are shown in Fig. 3. At the lower n values, the spectra exhibit a rich structure that extends over a broad wave-number range. As n increases, these structures become narrower and eventually coalesce into single lines located near the ionic transitions, indicated by the vertical lines. The spectra for the $3s60d$ and $3s80d$ states were recorded at higher laser pulse energies to compensate for the $1/n^3$ dependence of the excitation probability from the $3s^2$ ground state to the Rydberg states. Consequently, saturation and power broadening effects are more pronounced in these spectra.

The overall shape of these spectra can be qualitatively described using the ICE shakeup model [7,9]. The simplest case corresponds to the photoexcitation of a $3snd\ ^1D_2$ initial Rydberg state to a single $(3p_{1/2}n'd_j)_J$ core-excited Rydberg series coupled to a single continuum $(3s_{1/2}\epsilon d_j)_J$. Within the independent electron approximation, the two-electron wave functions of the initial and final states are expressed as products of the inner- and Rydberg-electron wave functions. Moreover, it is assumed that the dipole matrix elements $\langle \epsilon l | \boldsymbol{\mu}_2 | nd \rangle$ with $l = 1, 3$ corresponding to the direct photoionization of the Rydberg electron are negligible compared to the dipole matrix element $\langle 3p_{1/2} | \boldsymbol{\mu}_1 | 3s_{1/2} \rangle$ corresponding to the core-excitation transition. $\boldsymbol{\mu}_1$ and $\boldsymbol{\mu}_2$ are the transition dipole moments associated with the first and second electrons, respectively. The photoionization cross section of the $3snd$ Rydberg states can therefore be approximated by

$$\sigma_{\text{ICE}}(\omega) \simeq \frac{4\pi^2\omega}{c} |\langle 3p_{1/2} | \boldsymbol{\mu}_1 | 3s_{1/2} \rangle|^2 \times |\langle n^*d | n^*d \rangle|^2 A_{3p_{1/2}n'd_j}(\omega), \quad (12)$$

where ω is the angular frequency of the light, n^* and n'^* are the effective principal quantum numbers of the initial and final states, respectively, and $A_{3p_{1/2}n'd_j}$ is the spectral density of the

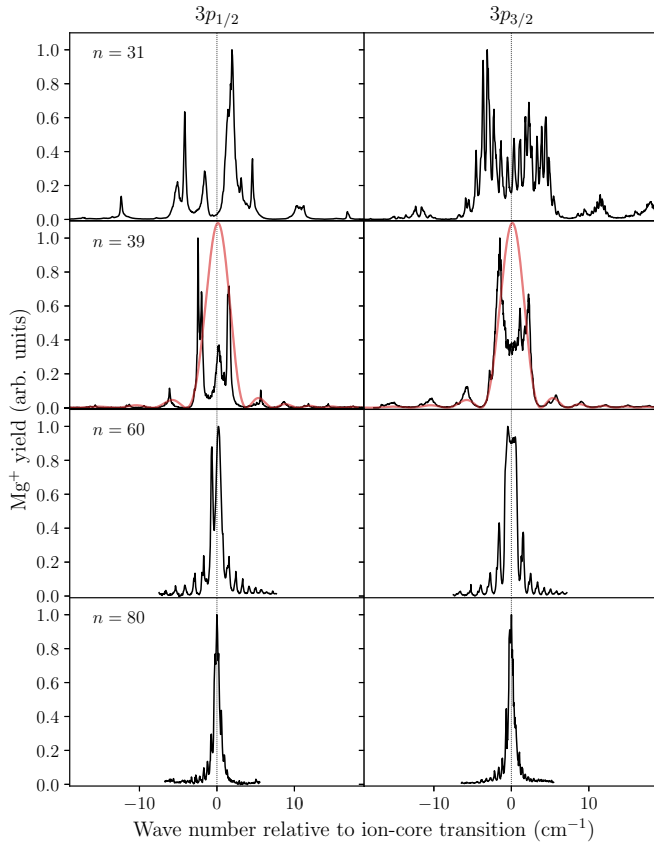


FIG. 3. Experimental $3s_{1/2} - 3p_{1/2}$ (left column) and $3s_{1/2} - 3p_{3/2}$ (right column) core-excitation spectra from the $3s31d$, $3s39d$, $3s60d$, and $3s80d$ Rydberg states of Mg. The red lines displayed for $n = 39$ represent the square of the ICE overlap integral [see Eq. (13) and text]. The left and right graphs shown in the upper row correspond to the regions labeled 1 and 1' in Fig. 1, respectively. Those in the second row from the top correspond to the regions labeled 2 and 2'. The graphs in the lowest two rows correspond to the regions labeled 3 (left column) and 3' (right column).

core-excited Rydberg series. The term $\langle 3p_{1/2} | \mu_1 | 3s_{1/2} \rangle$ can be taken, in good approximation, as the dipole matrix element of the $3s_{1/2} - 3p_{1/2}$ transition in the bare ion. It is independent of the photon energy $\hbar\omega$. The term $|\langle n^{*'}d | n^{*}d \rangle|^2$ corresponds to the shakeup of the Rydberg electron upon core excitation, and represents the square of the overlap between the initial and final Rydberg-electron wave functions. This overlap can be written to a good approximation as [52,53]

$$|\langle n^{*'}l | n^{*}l \rangle|^2 \simeq \frac{4(n^{*'}n^{*})^4}{n^{*3}(n^{*'} + n^{*})^2} \text{sinc}^2(n^{*'} - n^{*}), \quad (13)$$

where sinc is the normalized cardinal sine function. Equation (13) is shown for the case of $n = 39$ in Fig. 3 and matches the observed overall intensity distribution, particularly in the wings, which show a regular sequence of peaks with decreasing intensities as one moves away from the central region. The overlap integral has its maximum when the difference $\Delta n^{*} = n^{*'} - n^{*}$ between the initial and final effective principal quantum numbers of the Rydberg electron is zero, and vanishes when Δn^{*} has nonzero integer values. The side

bands reach their maximal values when Δn^{*} is half-integer and their amplitudes decrease with increasing Δn^{*} values. The spectral density of the autoionizing series, $A_{3p_{1/2}n'd_j}$, varies rapidly with the energy and is responsible for the detailed structure of the spectra. In the case of isolated Rydberg resonances, the spectral density would correspond to a series of Lorentzian-shaped lines with central positions given by Rydberg's formula. Deviations from this simple case, as observed in Fig. 3, are caused by the presence of multiple Rydberg series and ionization continua and their mutual interactions.

In the absence of perturbations, the autoionization rate of core-excited Rydberg states scales as $(n^{*'})^{-3}$ [22], a consequence of the reduced overlap between the core- and Rydberg-electron wave functions. The widths of individual resonances in the spectra thus decrease as n increases. The energy width of the overlap integral (13) also scales as $1/n^3$, resulting in a smaller energy spread of the central spectral structure. For example, its width is $\simeq 10 \text{ cm}^{-1}$ at $n = 31$ and reduces to about 0.6 cm^{-1} at $n = 80$. Because of the finite laser bandwidth, the entire spectral structure coalesces into a single line centered around the ion-core transition frequency, as expected from the rapid decoupling of the Rydberg electron from the ionic core when n increases. At very high n values, the autoionization rate of core-excited Rydberg states becomes comparable to, or even lower than, the fluorescence rate of the $3p$ state, in which case the width of the line corresponds to the natural line width of the ionic core transition [14,31].

B. Energies and widths of core-excited Rydberg states

We now turn to the quantitative analysis of the core-excitation spectra using the theoretical approach detailed in Sec. III. The calculated energies and widths of $(3p_{j_c}nd_j)_J$ core-excited Rydberg states with total angular momenta $J = 1$ and 3 are shown in Fig. 4. They correspond to the real part and twice the imaginary part of the eigenvalues of the complex-rotated Hamiltonian, respectively. Other series with the same values of J but different values of the orbital angular momentum of the Rydberg electron were also calculated, but are not shown for clarity. The assignments of the eigenstates to particular channels are carried out by inspecting the CI expansion coefficients. They can be ambiguous when eigenstates have almost equal contributions from different channels, which is typically the case in the energy ranges where channel interactions are dominant.

For $J = 3$, one series $(3p_{1/2}nd_{5/2})$ converges to the $3p_{1/2}$ ionization threshold, marked by the left full vertical line in Fig. 4, and two series $(3p_{3/2}nd_{3/2})$, $(3p_{3/2}nd_{5/2})$ converge to the $3p_{3/2}$ threshold, marked by the right full vertical line. The calculated thresholds are shifted to lower energies relative to the physical thresholds because of the truncation of the r_2 values in the calculation, which prevents the treatment of Rydberg states with n larger than $\simeq 90$. The shift relative to the measured threshold [17] is thus of the order of the binding energy of the $3p_{j_c}90d_j$ state, i.e., approximately $-1/(2 \times 90^2)$ hartree. Above these effective thresholds lie complex-rotated continuum states, marked by the orange circles. Similar considerations apply for $J = 1$, with the main difference that the $(3p_{1/2}nd_{5/2})$ series is replaced by the $(3p_{1/2}nd_{3/2})$ one.

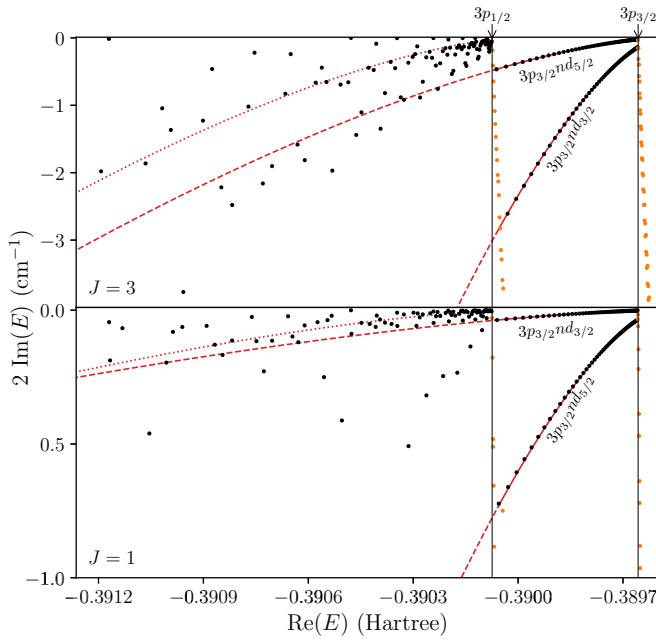


FIG. 4. Calculated energies and widths of core-excited $(3p_{j_c}nd_{j_c})_J$ Rydberg states for $J = 1$ and 3 (black circles). The rotated continuum states are indicated by the orange circles. The vertical lines indicate the positions of the calculated $\text{Mg}^+(3p_{1/2})$ and $\text{Mg}^+(3p_{3/2})$ ionization thresholds (see text). The full red lines show the $(n^*)^{-3}$ scaling of the autoionization rates of the $(3p_{3/2}nd_{j_c})_J$ Rydberg series above the $3p_{1/2}$ threshold. Their extrapolation below threshold is shown by the dashed red lines. The dotted red lines show the overall $(n^*)^{-3}$ evolution of the autoionization rates of the $(3p_{1/2}nd_{j_c})_J$ series.

Two different regimes are observable in Fig. 4. Above the $3p_{1/2}$ threshold, the two Rydberg series converging to the $3p_{3/2}$ threshold exhibit regular, unperturbed progressions. Their energies follow Rydberg's formula and the associated quantum defects can be obtained (modulo 1) from a fit with Eq. (9) using Ritz's expansion of the quantum defects up to the second order [22]:

$$\delta(n) = \delta_0 - \frac{\delta_2}{(n - \delta_0)^2}. \quad (14)$$

The results of the fit are given in Table I for all calculated Rydberg series with $J = 1-3$ converging to the $3p_{3/2}$ threshold. The autoionization widths of these series scale as $(n^*)^{-3}$, as shown by the full red curves in Fig. 4. The scaling factor γ , called the scaled autoionization width, is obtained from a fit based on the equation

$$\Gamma_n = \frac{\gamma}{[n - \delta(n)]^3}, \quad (15)$$

and the calculated widths, and is also given in Table I.

Below the $3p_{1/2}$ threshold, the Rydberg series do not exhibit a regular behavior because of interactions between series converging to the $3p_{1/2}$ and $3p_{3/2}$ thresholds. Series having the same J value but different values of l_c , j_c , l , and j are coupled by the Coulomb repulsion between the two electrons, i.e., by the $1/r_{12}$ operator in Eq. (1). The extent of this coupling depends on the angular momenta and

TABLE I. Quantum defects δ_0 and δ_2 and scaled autoionization rates (γ) of the Rydberg series with $J = 1-3$ converging to the $3p_{3/2}$ threshold (see text for details).

Series	δ_0	δ_2	γ/cm^{-1}
$(3p_{3/2}ns_{1/2})_1$	0.58	0.24	27949.49
$(3p_{3/2}ns_{1/2})_2$	0.63	-0.02	1639.78
$(3p_{3/2}np_{1/2})_1$	0.11	1.43	572.32
$(3p_{3/2}np_{1/2})_2$	0.14	1.35	33683.72
$(3p_{3/2}np_{3/2})_1$	0.22	0.62	4893.71
$(3p_{3/2}np_{3/2})_2$	0.12	1.28	11013.11
$(3p_{3/2}np_{3/2})_3$	0.22	0.74	6162.29
$(3p_{3/2}nd_{3/2})_1$	0.17	1.54	1295.85
$(3p_{3/2}nd_{3/2})_2$	0.18	1.46	2733.12
$(3p_{3/2}nd_{3/2})_3$	0.04	4.73	101900.38
$(3p_{3/2}nd_{5/2})_1$	0.99	0.56	25985.07
$(3p_{3/2}nd_{5/2})_2$	0.31	0.42	7401.74
$(3p_{3/2}nd_{5/2})_3$	0.22	1.29	16343.80
$(3p_{3/2}nf_{5/2})_1$	0.99	0.19	1493.88
$(3p_{3/2}nf_{5/2})_2$	0.06	2.13	5125.69
$(3p_{3/2}nf_{5/2})_3$	0.09	1.87	3565.04
$(3p_{3/2}nf_{7/2})_1$	0.99	0.19	1132.15
$(3p_{3/2}nf_{7/2})_2$	0.05	2.05	5823.28
$(3p_{3/2}ng_{7/2})_1$	0.99	0.06	123.83
$(3p_{3/2}ng_{7/2})_2$	0.02	2.15	1021.09
$(3p_{3/2}ng_{9/2})_1$	0.99	0.06	110.73
$(3p_{3/2}nh_{9/2})_1$	0.99	-0.01	3.50

on the details of the wave functions at small r values. The interactions occur over the whole range of energies shown in Fig. 4. This behavior is in contrast with that observed in the heavier alkaline-earth-metal elements, for which the perturbations are often more localized [2,14], and is the result of the smaller fine-structure splitting of the $3p_{1/2}$ and $3p_{3/2}$ thresholds (91.57 cm^{-1} [17]), which implies a larger density of $3p_{3/2}nd_{j_c}$ states below the $3p_{1/2}$ threshold.

A more detailed analysis of the series perturbations requires the inspection of the CI coefficients. For $J = 1$, the vast majority of the $3p_{1/2}nd_{3/2}$ states are mixed with members of the $3p_{3/2}nd_{5/2}$ series throughout the energy range shown in Fig. 4. This mixing is so extensive that no state belonging predominantly to the $3p_{3/2}nd_{5/2}$ series can be identified in the range from -0.3903 hartree to the $3p_{1/2}$ threshold. Mixing of the $3p_{1/2}nd_{3/2}$ series with the $3p_{3/2}nd_{3/2}$ series is localized to only a few $3p_{1/2}nd_{3/2}$ states, indicating a much weaker series interaction. The CI coefficients also indicate a mixing between the $3p_{1/2}nd_{3/2}$ and $3p_{3/2}ns_{1/2}$ series, although less extensive than with the $3p_{3/2}nd_{5/2}$ series. The perturbations observed in the part of the spectrum below the $3p_{1/2}$ threshold arise from the same interactions as those responsible for the autoionization into $3p_{1/2}\epsilon l_j$ continua above this threshold. Consequently, the widths of the $3p_{3/2}nd_{5/2}$ series, which reflect below the $3p_{1/2}$ threshold the rate of autoionization into the $3s_{1/2}\epsilon l_j$ continua, abruptly increase by about an order of magnitude when the $3p_{1/2}$ threshold is crossed and the $3p_{1/2}\epsilon l_j$ continua become energetically accessible. The strong $3p_{1/2}nd_{3/2} - 3p_{3/2}nd_{5/2}$ interaction is therefore responsible for the fast spin-orbit autoionization of the latter states. In contrast, the $3p_{3/2}nd_{3/2}$ series, which does not interact strongly with the $3p_{1/2}nd_{3/2}$ series below threshold, does not exhibit

a similar increase of the autoionization width. Indeed, the autoionization rates of $3p_{3/2}nd_{3/2}$ states just below the $3p_{1/2}$ threshold are close to the rates predicted by Eq. (15) with a scaled rate determined from the properties of this Rydberg series above threshold (see dashed red line in Fig. 4). We therefore conclude that the autoionization of $3p_{3/2}nd_{3/2}$ states into the $3p_{1/2}\epsilon l_j$ continua is slower than into the $3s_{1/2}\epsilon l_j$ ones. For $J = 3$ the situation is reversed, and the $3p_{1/2}nd_{5/2}$ series couples strongly to the $3p_{3/2}nd_{3/2}$ series, whereas the interaction with the $3p_{3/2}nd_{5/2}$ series is weaker. The opening of the continua above the $3p_{1/2}$ threshold thus leads to a very large increase of the autoionization widths of the members of the $3p_{3/2}nd_{3/2}$ series, which are characterized by the largest of all calculated scaled widths (see Table I).

The autoionization widths of $J = 3$ states are also significantly larger than those of $J = 1$ states, as already noticed and explained by Schinn *et al.* with the help of a simple hydrogenic model [16]. Because of parity conservation, $(3p_j\epsilon nd_j)_1$ states located below the $3p_{1/2}$ threshold can only decay into $(3s_{1/2}\epsilon p_{1/2,3/2})_1$ continua, while $(3p_j\epsilon nd_j)_3$ states can only do so into $3s_{1/2}\epsilon f_{5/2,7/2}$ continua. Schinn *et al.* showed that hydrogenic Rydberg nd wave functions associated with a $3p$ core have a stronger overlap with ϵf continuum wave functions associated with the $3s$ core than with ϵp ones. This behavior results from the difference in energy between the $3s$ and $3p$ core states, and the different centrifugal barriers of the p and f channels [16].

The energies and widths of $(3p_j\epsilon nd_j)_{J=1,3}$ states thus provide insight into the structure and decay dynamics of core-excited Rydberg states. In particular, we identified a dominant interaction between the $(3p_{1/2}nd_{J-1/2})_J$ and $(3p_{3/2}nd_{3-J/2})_J$ series that induces strong perturbations below the $3p_{1/2}$ threshold over a broad range of n values and an abrupt and large increase of the autoionization widths of the $(3p_{3/2}nd_{3-J/2})_J$ series above the $3p_{1/2}$ threshold.

C. Theoretical and experimental core-excitation spectra

The experimental spectrum of the $3s_{1/2} - 3p_{1/2}$ core transition recorded from the $3s31d^1D_2$ Rydberg state is compared in Fig. 5 with the theoretical spectrum calculated using Eq. (11). This spectral range corresponds to the region labeled 1 in Fig. 1. The overall agreement between the two spectra is excellent over the whole wave-number range: the resonance positions agree to better than 0.1 cm^{-1} and the widths of the broadest resonances in the calculated spectrum perfectly match those observed experimentally. The widths of the narrowest resonances appear slightly underestimated by the calculation, which is primarily a result of saturation and power broadening, which are not accounted for in the calculation. The effects of saturation and power broadening are also noticeable in the relative intensities: whereas the sharpest lines appear more intense in the calculated spectrum than in the experimental spectrum, their integrated intensities are almost identical. We attribute the remaining small discrepancies between the experimental and calculated spectra to small drifts of the Mg-atom density, inaccuracies in the model potential, and the neglect of dynamical interactions with the Mg^{2+} core.

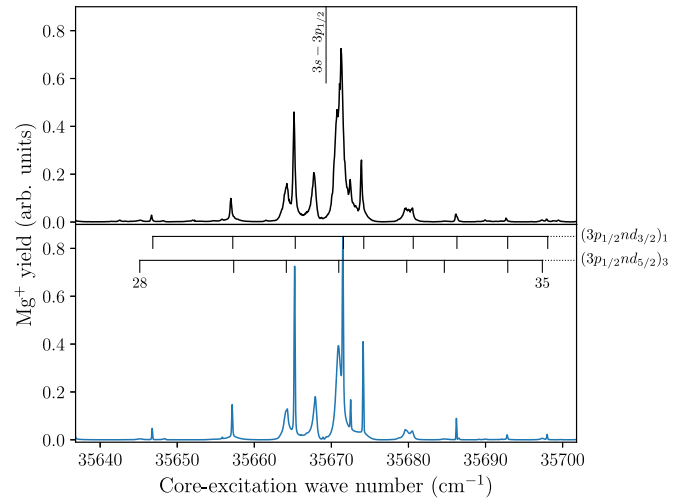


FIG. 5. Experimental (top) and calculated (bottom) $3s_{1/2} - 3p_{1/2}$ core-excitation spectra from the $3s31d^1D_2$ Rydberg state. The vertical line shows the position of the $3s_{1/2} - 3p_{1/2}$ transition in the bare ion. The calculated positions of $(3p_{1/2}nd_j)_J$ resonances are shown in the assignment bar in the lower panel.

This excellent agreement enables one to unambiguously attribute every peak in the photoionization spectrum to a core-excited Rydberg state. This is achieved by decomposing the photoionization cross section into contributions corresponding to $J = 1, 2$, and 3 , as shown in Fig. 6. The cross section for $J = 1$ exhibits a number of narrow resonances with energies and widths corresponding to those of $3p_{1/2}nd_{3/2}$ states. Series perturbations are apparent in the irregular intensity distribution and intervals between successive members of the series. The cross section for $J = 2$ consists of a series of pairs of lines, the lower one being significantly broader than the upper one, and which can be attributed to the $3p_{1/2}nd_{3/2}$ and $3p_{1/2}nd_{5/2}$ series, respectively. The Rydberg progressions appear less perturbed than for $J = 1$. Resonances marked by an arrow are $3p_{3/2}nd_j$ perturber states that gain intensity through channel interactions.

The cross section for $J = 3$ exhibits the most complex patterns. The widths of most peaks are significantly larger than for $J = 1$ because of the increased autoionization rates of $J = 3$ states (see Fig. 4 and Sec. IV B). The broadest resonances, indicated by the open circles, can be assigned to the $3p_{1/2}nd_{5/2}$ series. Sharp resonances are also observed in the cross section and are marked by triangles in Fig. 6. They correspond to $3p_j\epsilon ng_j$ resonances, which exhibit Beutler-Fano profiles instead of the Lorentzian profiles expected in ICE spectra. An example of such resonances is shown in the inset of Fig. 6 and corresponds to a Fano q parameter of -0.35 . Because the direct photoionization of the Rydberg nd electron is negligible, the interferences responsible for these profiles must result from the interactions between the $3p_j\epsilon nd_j$ and $3p_j\epsilon ng_j$ discrete states and the $3s\epsilon f_j$ continua. Although they appear sharp in the theoretical cross section, the lines associated with $3p_j\epsilon ng_j$ resonances are much narrower than the laser bandwidth and have very small integrated line strengths. They are therefore not observed in the experimental spectrum in Fig. 5. The resonances in the $J = 3$ cross section marked with arrows in Fig. 6 correspond to $3p_{3/2}nd_j$ perturber states.

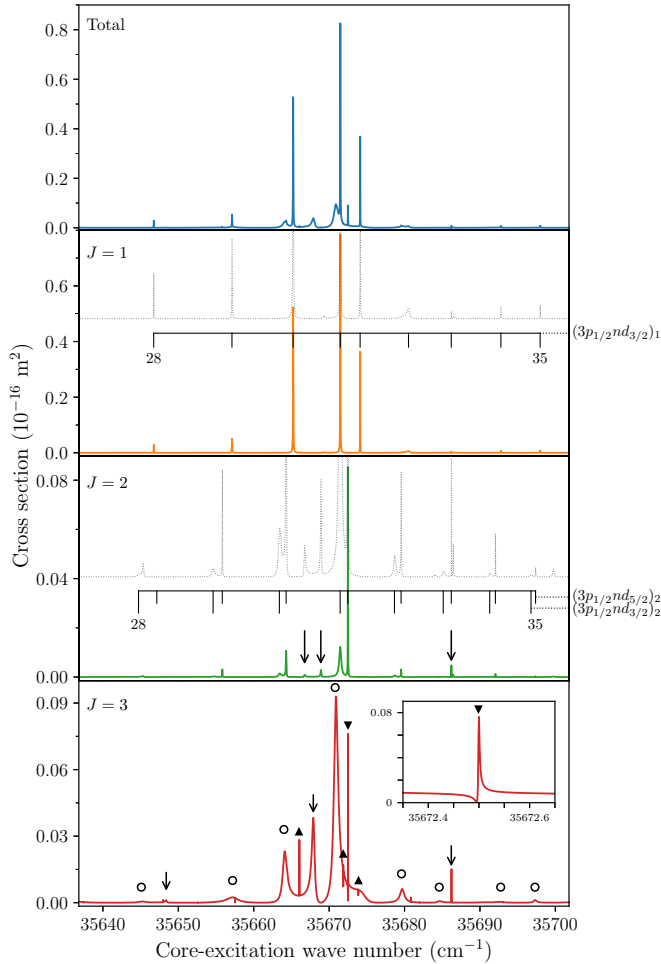


FIG. 6. Theoretical $3s_{1/2} - 3p_{1/2}$ core-excitation cross sections from the $3s31d\ ^1D_2$ Rydberg state. The top panel shows the total cross section, while the lower ones show the partial cross sections to final states with total angular momenta $J = 1, 2,$ and 3 , respectively. The gray, dotted lines in the second and third panels show the same cross sections as the full lines but on an enlarged vertical scale and with a vertical offset for clarity. In these panels, the assignment of resonances to given Rydberg series is shown by the horizontal assignment bar. Vertical arrows indicate the positions of the strongest perturber states. Empty circles in the lower panel ($J = 3$) show the positions of $3p_{1/2}nd_{5/2}$ resonances. Full triangles indicate resonances associated with $3p_{1/2}ng_j$ states. One of these resonances is marked with an inverted triangle and is shown in the inset on an enlarged horizontal scale.

The present theoretical approach provides absolute values of the core-excitation cross section which do not rely on the ICE approximations discussed in Sec. IV A and formulas analogous to Eq. (12). Absolute cross sections have not been reported in the literature before, presumably because of the absence of absolute experimental measurements. The core-excitation cross section from the $3s31d$ Rydberg state, shown in Fig. 6, is more than five orders of magnitude larger than that of the photoionization of ground-state atoms in the same range of final, core-excited Rydberg states. Indeed, we estimate from Ref. [54] that the latter cross section lies below 10^{-22} m². This large difference can be explained by the

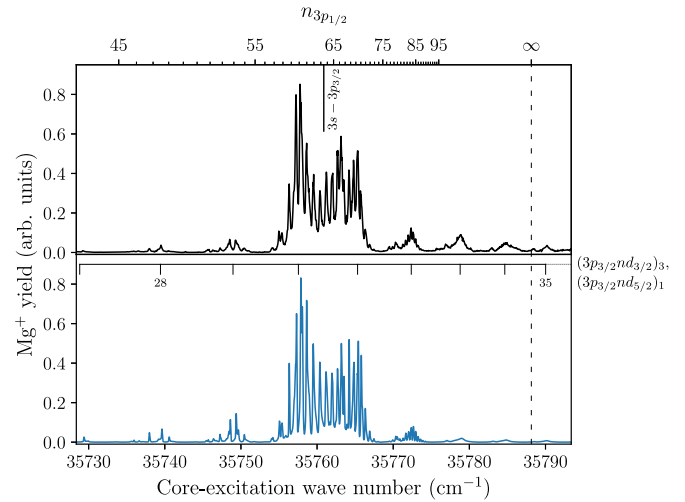


FIG. 7. Experimental (top) and calculated (bottom) $3s_{1/2} - 3p_{3/2}$ core-excitation spectra from the $3s31d\ ^1D_2$ Rydberg state. The full vertical line shows the position of the $3s_{1/2} - 3p_{3/2}$ ionic transition. The dashed vertical line indicates the position of the $3p_{1/2}$ threshold. The values of principal quantum numbers relative to that threshold are indicated on the scale located on the upper horizontal axis. The positions of $(3p_{3/2}nd_{5/2})_1$ and $(np_{3/2}nd_{3/2})_3$ resonances, determined from the quantum defects given in Table I, are shown in the assignment bar in the lower panel.

fact that the excitation of core-excited Rydberg states from the ground state involves the simultaneous excitation of two electrons, one of which goes to a high-lying Rydberg state, whereas the ICE process involves the excitation of a single electron through a strong, low-lying electronic transition of the ion core. The overall magnitude of the core-excitation cross section does not vary significantly as n increases, highlighting the fact that the strength of the excitation is a property of the ion core.

The experimental and theoretical spectra of the $3s_{1/2} - 3p_{3/2}$ core transition recorded from the $3s31d$ state are shown in Fig. 7. They correspond to the region labeled $1'$ in Fig. 1. The agreement between theory and experiment is again excellent, with the exception of the resonances on the high-energy side of the spectrum, which appear weaker in the calculated spectrum than in the experimental spectrum. The spectra consist of a few broad resonances attributed to $3p_{3/2}nd_j$ states with effective principal quantum numbers in the range from 27 to 35, on top of which a large number of narrow resonances are superimposed. These latter resonances can be attributed to high-lying members of the $3p_{1/2}nd_j$ series converging to the $3p_{1/2}$ threshold, and to several $(3p_{1/2}ns_{1/2})_1$ perturbers. The effective principal quantum numbers associated with these states are in the range from $\simeq 45$ to $\simeq 95$, as indicated along the upper horizontal axis of Fig. 7. In the absence of channel interactions, the excitation from the $3s31d$ state to $3p_{1/2}nd_j$ states with, e.g., $n^* \simeq 65$ is very unlikely because the efficiency of the shakeup of the Rydberg electron decreases rapidly with the effective principal quantum number difference $\Delta n^* = n^{*'} - n^*$, as discussed in Sec. IV A. Indeed, the overlap integral given by Eq. (13) is smaller by a factor of 8×10^{-5} for $\Delta n^* \simeq 34$ compared to its value for $\Delta n^* \simeq 0$. The presence of $3p_{1/2}nd_j$ resonances in the spectra is

therefore the result of the strong interactions between series converging to the $3p_{1/2}$ and $3p_{3/2}$ thresholds. For n^* values larger than $\simeq 95$, individual members of the $3p_{1/2}nd_j$ series are no longer resolved experimentally. Our calculations only describe Rydberg states up to $n \simeq 90$, as explained in Sec. III, and states with higher energies are calculated as continuum states. The discrete Rydberg series thus turn into quasicontinua. Resonances above the $3p_{1/2}$ threshold, indicated by the dashed vertical line in Fig. 7, exhibit shapes similar to those of resonances located just below threshold, where the high-lying Rydberg series are unresolved: the interaction of $3p_{3/2}nd_j$ states with the $3p_{1/2}nd_{j'}$ quasicontinua is indeed identical to their interaction with true $3p_{1/2}\epsilon d_{j'}$ continua.

Similar spectra showing the interaction of low-lying Rydberg states with high-lying members of another series have been recorded and analyzed earlier in Sr [55] and Ba [56–58]. In such cases, the principal quantum number of the $n_c p_{3/2}nl$ Rydberg state is lower ($n \simeq 10$) than in the present case and so are those of the perturber series ($3p_{1/2}nl$ with $n \simeq 10$ –30). Schinn *et al.* [16] have calculated a qualitatively similar spectrum for the photoionization of Mg($3s30d$), however, the narrow structures associated with $3p_{1/2}nd_j$ states could not be resolved in their experimental spectra. The mixing of low- n , rapidly autoionizing $3p_{3/2}nd_j$ states with high-lying $3p_{1/2}n'd_{j'}$, with much smaller autoionization rates, stabilizes the former states. If n' is sufficiently large, the autoionization rate becomes comparable to the fluorescence rate of the core electron ($2.60 \times 10^8 \text{ s}^{-1}$ [17]) and the core-excited states radiatively decay to singly excited Rydberg states [31]. Such a stabilization of autoionizing states was investigated in Ba by Story *et al.* [59] and Ereifej and Story [60]. This phenomenon is analogous to that leading to intensity perturbations observed in pulsed-field-ionization zero-kinetic-energy photoelectron spectra of, e.g., the N_2 molecule [61].

Figure 8 compares the measured and calculated $3s_{1/2} - 3p_{1/2}$ core-excitation spectra from the $3s39d \ ^1D_2$ Rydberg

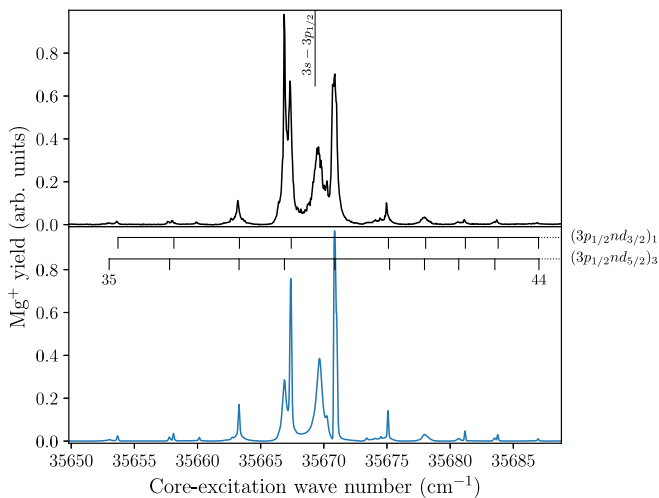


FIG. 8. Experimental (top) and calculated (bottom) $3s_{1/2} - 3p_{1/2}$ core-excitation spectra from the $3s39d \ ^1D_2$ Rydberg state. The vertical line shows the position of the $3s_{1/2} - 3p_{1/2}$ ionic transition. The calculated positions of $(3p_{1/2}nd_j)_j$ resonances are shown in the assignment bar in the lower panel.

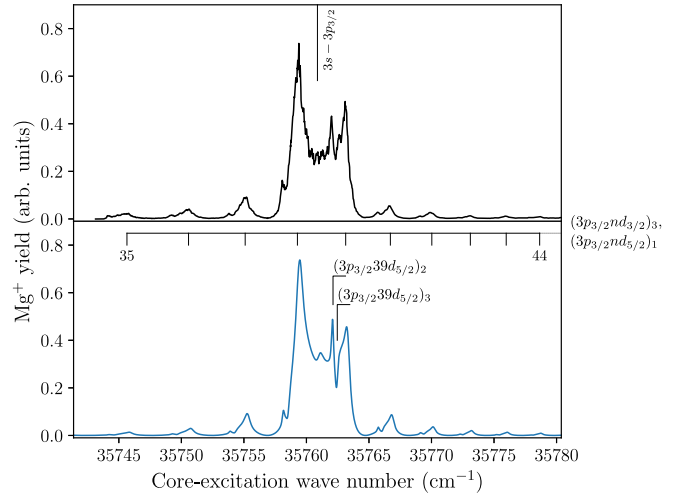


FIG. 9. Experimental (top) and calculated (bottom) photoionization spectra of the $3s39d \ ^1D_2$ Rydberg state in the vicinity of the $3s_{1/2} - 3p_{3/2}$ core resonance. The vertical line shows the position of the $3s_{1/2} - 3p_{3/2}$ ionic transition. The calculated positions of $(3p_{3/2}nd_{5/2})_1$ and $(np_{3/2}nd_{3/2})_3$ resonances are shown in the assignment bar in the lower panel. They are degenerate on the scale of the figure. Two vertical lines in the lower panel indicate the calculated positions of the $(3p_{3/2}39d_{5/2})_2$ and $(3p_{3/2}39d_{5/2})_3$ resonances in the central spectral feature.

state, corresponding to the region labeled 2 in Fig. 1. The theoretical spectrum is in excellent agreement with the experimental one, and even the weakest features are well reproduced by the calculation. The only difference concerns the amplitudes of the two resonances around 35667 cm^{-1} , which are inverted in the calculated spectrum. The main characteristics of the spectra are similar to those already discussed for the $3s31d$ state.

Spectra of the $3s_{1/2} - 3p_{3/2}$ core transition from the $3s39d$ state are shown in Fig. 9 and correspond to the region labeled 2' in Fig. 1. All resonances in these spectra are located energetically above the $3p_{1/2}$ threshold, and the multiple sharp structures associated with the coupling to high- n $3p_{1/2}n'd_{j'}$ states in the case of the $3s31d$ state (see Fig. 7) have now turned into a smooth profile resulting from autoionization into $3p_{1/2}\epsilon d_{j'}$ continua. The spectra consist of a series of broad lines on top of which sharper structures can be discerned. The broad resonances can be attributed to $(3p_{3/2}nd_{3/2})_3$ states, which rapidly and predominantly autoionize into the $3p_{1/2}\epsilon d_{5/2}$ continuum. The 1.72-cm^{-1} width of the $(3p_{3/2}39d_{3/2})_3$ state is of the order of half the spacing between adjacent Rydberg states at $n = 39$ (3.57 cm^{-1}), so that the spectral density of $(3p_{3/2}nd_{3/2})_3$ states is essentially flat. Consequently, the shape of the broad features in the spectra is not governed by the detailed profile of the individual resonances but rather by the sinc^2 -type shape of the overlap integral itself (see discussion in Sec. IV A). Dips, such as the one observed on the right of the isolated ion-core resonance (vertical line in Fig. 9), correspond to the positions of $(3p_{3/2}nd_{5/2})_3$ resonances. The narrow resonance on its left, marked by another vertical line, can be unambiguously assigned to a $(3p_{3/2}nd_{5/2})_2$ resonance, and made it necessary

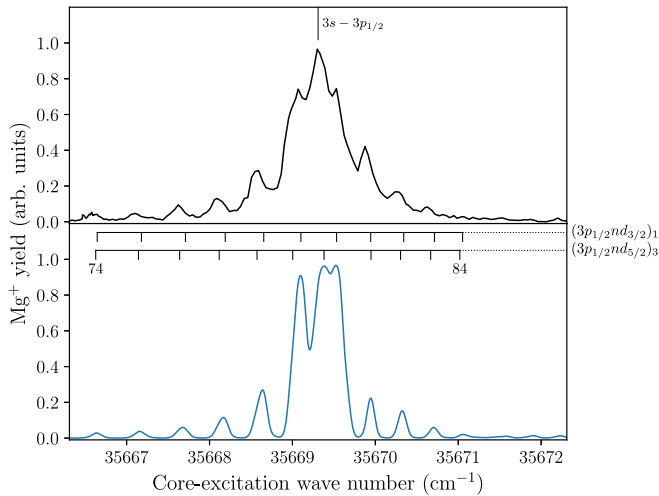


FIG. 10. Experimental (top) and calculated (bottom) photoionization spectra of the $3s80d\ ^1D_2$ Rydberg state in the vicinity of the $3s_{1/2} - 3p_{1/2}$ core resonance. The vertical line shows the position of the $3s_{1/2} - 3p_{1/2}$ ionic transition. The calculated positions of $(3p_{1/2}nd_j)_J$ resonances are shown in the assignment bar in the lower panel.

to add a small $J = 2$ component to the total cross section (see Sec. III). The other resonances can be attributed to $(3p_{3/2}nd_j)_1$ resonances, as indicated along the assignment bar.

The spectra of the $3s_{1/2} - 3p_{1/2}$ and $3s_{1/2} - 3p_{3/2}$ ion-core transitions recorded from the $3s80d$ Rydberg state are shown in Figs. 10 and 11. They correspond to the regions labeled 3 and 3' in Fig. 1. The overall agreement between theory and experiment is good, although the shape of the central peak is not as well reproduced as in regions 1, 1', 2 and 2'. In the experiment, residual stray fields have induced a small Stark mixing of high-lying Rydberg states that modified the autoionization dynamics of core-excited Rydberg states

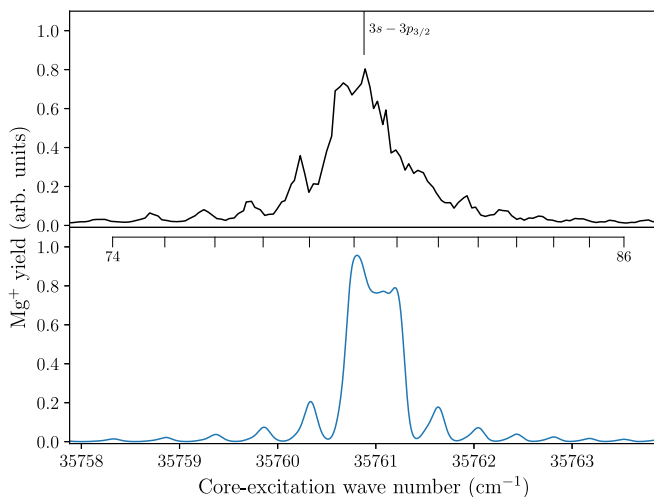


FIG. 11. Experimental (top) and calculated (bottom) photoionization spectra of the $3s80d\ ^1D_2$ Rydberg state in the vicinity of the $3s_{1/2} - 3p_{3/2}$ core resonance. The vertical line shows the position of the $3s_{1/2} - 3p_{3/2}$ ionic transition. The calculated positions of $(3p_{3/2}nd_j)_J$ are shown in the assignment bar in the lower panel.

as explained in Ref. [31]. The influence of residual power broadening on the shape of these narrow spectra is also more pronounced. In the calculations, the description of Rydberg states with principal quantum numbers as large as $n \simeq 80$ is challenging, and small inaccuracies in the positions of the resonances also affect the overall shape of the spectrum.

Resonances associated with the core-excited Rydberg series are not well resolved in Figs. 10 and 11, and bundle into a single feature for each value of the principal quantum number n . Consequently, the widths of the different lines are much larger than the autoionization widths of most states and are limited by spectral congestion and the laser bandwidth. Without convolution by the experimental line-shape function, the theoretical cross section in the $3s_{1/2} - 3p_{3/2}$ region (not shown) is almost identical to that for the $3s39d$ Rydberg state.

V. DISCUSSION AND CONCLUSIONS

The spectra of the $3s_{1/2} - 3p_{j_c}$ ($j_c = 1/2, 3/2$) ion-core transitions of Mg recorded from a broad range of $3snd\ ^1D_2$ Rydberg states reveal a rich behavior and complex patterns of resonances. To fully characterize the relevant processes, large-scale calculations of the spectra have been carried out using a configuration-interaction approach combined with the exterior-complex-scaling method. Experiments and calculations were performed in the regions below the $3p_{1/2}$ ionization threshold, where the $(3p_{j_c}nd_j)_J$ resonances decay by autoionization in the $(3s_{1/2}\epsilon l_j)_J$ continua, and between the $3p_{1/2}$ and $3p_{3/2}$ thresholds, where spin-orbit autoionization also affects the dynamics of the $(3p_{3/2}nd_j)_J$ Rydberg series. The overall excellent agreement between theory and experiment validates the configuration-interaction exterior-complex-scaling approach to treat core-excited Rydberg states. The calculations faithfully reproduce the positions, widths, shapes, and relative amplitudes of the resonances up to principal quantum numbers much beyond 50. Series interactions, which are ubiquitous for Rydberg series below the $3p_{1/2}$ threshold, are quantitatively reproduced, which indicates that electron-electron correlations are correctly accounted for. Inclusion of the spin-orbit interaction, usually neglected in analogous calculations in helium [10–13], does not cause additional difficulties when jj coupling is used.

The autoionization of the $3p_{3/2}nd_j$ states of Mg above the $3p_{1/2}$ threshold is similar to the autoionization of the $n_c p^5(^2P_{1/2})nd$ Rydberg states of rare gases: both processes result in the emission of a Rydberg d electron into the continua above the lower spin-orbit component ($np^5\ ^2P_{3/2}$ or $3p\ ^2P_{1/2}$) of the corresponding ion. There are, however, two differences: (i) in the rare gases, the $^2P_{3/2}$ ionization threshold lies lower in energy than the $^2P_{1/2}$ threshold, whereas the contrary is true for Mg; (ii) core-excited Rydberg states of Mg can also autoionize into $3s_{1/2}nl_j$ continua, whereas the $^2P_{3/2}$ threshold of the rare gases is the lowest ionization threshold. However, we showed that for some series of Mg the coupling of $3p_{3/2}nd_j$ states to $3p_{1/2}\epsilon d_j$ continua represents the dominant interaction. The spin-orbit autoionization in the rare gases, leaving the ion in the $^2P_{3/2}$ ground state, is considered as an example of very efficient autoionization [62,63]. The scaled autoionization rate of the $(3p_{3/2}nd_{3/2})_3$ series of Mg ($101\,900.38\text{ cm}^{-1}$) also falls in this category, as it is larger by

a factor of 3 compared to the largest scaled rate measured in the rare gases [64]. The lifetime associated with this rate (27 ps for $n = 80$) is even smaller than the classical orbit period of the Rydberg electron (78 ps for $n = 80$). Such large rates have also been observed in heavier alkaline-earth-metal atoms (see Refs. [55,65] for examples in Sr).

In line with previous studies [2], the present results also show that the autoionization rates of core-excited Rydberg states strongly depend not only the principal and orbital angular momenta of the Rydberg electron, but also on its total angular momentum j and on the total angular momentum J of the system. For example, the scaled autoionization width of $(3p_{3/2}np_{1/2})_1$ states ($\gamma = 572.32 \text{ cm}^{-1}$) is twice smaller than that of the $(3p_{3/2}ng_{7/2})_3$ ones ($\gamma = 1021.09 \text{ cm}^{-1}$), although the orbital angular momentum of the outer electron in the latter case is significantly larger. For experiments requiring long-lived core-excited Rydberg states, such as the applications in quantum optics discussed in the Introduction, it is therefore relevant to carefully consider not only n and l , but also j and J . Selecting a particular j value may be difficult because in most cases resonances associated with different values of l and j overlap. Nonetheless, the value of J can be selected and changed by, e.g., modifying the polarization of the excitation lasers or the excitation scheme to the initial, singly excited Rydberg states. The latter possibility may involve exciting the Rydberg states no longer from the ground state of the atom but from a metastable state, such as the $nsnp^3P_{0,1,2}$ states of the alkaline-earth-metal atoms ($n = 2$ to 6 from Be to Ba).

Finally, we demonstrated that the present theoretical approach to treat core-excited Rydberg states represents an alternative to the R -matrix MQDT method widely used in previous works, and provides complementary information. The approach yields, among others, the eigenvectors of the two-electron Hamiltonian, and provides the energies and widths of resonances even in regions where these strongly overlap. It does not rely on the approximations inherent to MQDT, such as assuming that the Rydberg electron experiences only the Coulomb potential of the ion core at large radial distances, and includes channels that were previously neglected [15,16], in particular, the $3p_{j_c}ng_j$ channels. These channels give rise to resonances with asymmetric Beutler-Fano profiles that had neither been calculated nor observed before. The results of our calculations are overall in good agreement with the experimental and R -matrix-MQDT-based results of Dai *et al.* and Schinn *et al.* [15,16], and confirm from first principles the validity of the ICE approximations at high n values.

ACKNOWLEDGMENTS

We thank J. A. Agner and H. Schmutz for their contribution to the development of the spectrometer used in this study. This work is supported financially by the Swiss National Science Foundation (Grant No. 200020-172620) and the European Research Council for an advanced grant under the European Union's Horizon 2020 research and innovation programme (Grant No. 743121).

-
- [1] G. Tanner, K. Richter, and J.-M. Rost, *Rev. Mod. Phys.* **72**, 497 (2000).
 - [2] M. Aymar, C. H. Greene, and E. Luc-Koenig, *Rev. Mod. Phys.* **68**, 1015 (1996).
 - [3] S. J. Buckman and C. W. Clark, *Rev. Mod. Phys.* **66**, 539 (1994).
 - [4] H. Beutler, *Z. Phys.* **93**, 177 (1935).
 - [5] U. Fano, *Phys. Rev.* **124**, 1866 (1961).
 - [6] R. Wehlitz, D. Lukić, and P. N. Juranić, *J. Phys. B: At., Mol. Opt. Phys.* **40**, 2385 (2007).
 - [7] W. E. Cooke, T. F. Gallagher, S. A. Edelstein, and R. M. Hill, *Phys. Rev. Lett.* **40**, 178 (1978).
 - [8] W. E. Cooke, in *Atomic Physics 7*, edited by D. Kleppner and F. Pipkin (Springer, Boston, 1981), pp. 167–180.
 - [9] T. F. Gallagher, *J. Opt. Soc. Am. B* **4**, 794 (1987).
 - [10] Y. K. Ho and J. Callaway, *J. Phys. B: At. Mol. Phys.* **18**, 3481 (1985).
 - [11] A. Burgers, D. Wintgen, and J.-M. Rost, *J. Phys. B: At., Mol. Opt. Phys.* **28**, 3163 (1995).
 - [12] J.-M. Rost, K. Schulz, M. Domke, and G. Kaindl, *J. Phys. B: At., Mol. Opt. Phys.* **30**, 4663 (1997).
 - [13] G. Lagmago Kamta, B. Piraux, and A. Scrinzi, *Phys. Rev. A* **63**, 040502(R) (2001).
 - [14] G. Fields, X. Zhang, F. B. Dunning, S. Yoshida, and J. Burgdörfer, *Phys. Rev. A* **97**, 013429 (2018).
 - [15] C. J. Dai, G. W. Schinn, and T. F. Gallagher, *Phys. Rev. A* **42**, 223 (1990).
 - [16] G. W. Schinn, C. J. Dai, and T. F. Gallagher, *Phys. Rev. A* **43**, 2316 (1991).
 - [17] A. Kramida, Yu. Ralchenko, J. Reader, and NIST ASD Team, NIST Atomic Spectra Database (ver. 5.6.1) [online], Available: <https://physics.nist.gov/asd> [2019, January 29], National Institute of Standards and Technology, Gaithersburg, MD.
 - [18] M. D. Lindsay, L.-T. Cai, G. W. Schinn, C. J. Dai, and T. F. Gallagher, *Phys. Rev. A* **45**, 231 (1992).
 - [19] M. D. Lindsay, C. J. Dai, L.-T. Cai, T. F. Gallagher, F. Robicheaux, and C. H. Greene, *Phys. Rev. A* **46**, 3789 (1992).
 - [20] B. J. Lyons, J. A. Shanchuck, J. Hostetler, and T. F. Gallagher, *Phys. Rev. A* **52**, 4586 (1995).
 - [21] J. B. M. Warntjes, F. Robicheaux, and L. D. Noordam, *Phys. Rev. A* **62**, 033407 (2000).
 - [22] T. F. Gallagher, *Rydberg Atoms* (Cambridge University Press, Cambridge, 1994).
 - [23] R. Mukherjee, J. Millen, R. Nath, M. P. A. Jones, and T. Pohl, *J. Phys. B: At., Mol. Opt. Phys.* **44**, 184010 (2011).
 - [24] F. B. Dunning, T. C. Killian, S. Yoshida, and J. Burgdörfer, *J. Phys. B: At., Mol. Opt. Phys.* **49**, 112003 (2016).
 - [25] K.-L. Pham, H. Lehec, W. Maineult, S. Lepoutre, P. Pillet, T. F. Gallagher, and P. Cheinet, in *13th European Conference on Atoms, Molecules and Photons*, <https://www.ecamp13.org/sites/www.ecamp13.org/files/documenti/ecamp2019-abstract-book.pdf>.
 - [26] P. McQuillen, X. Zhang, T. Strickler, F. B. Dunning, and T. C. Killian, *Phys. Rev. A* **87**, 013407 (2013).
 - [27] G. Lochead, D. Boddy, D. P. Sadler, C. S. Adams, and M. P. A. Jones, *Phys. Rev. A* **87**, 053409 (2013).
 - [28] H. Lehec, Spectroscopie Rydberg et excitation du coeur isolé

- d'atomes d'ytterbium ultra-froids, Ph.D. thesis, Université de Paris Saclay, 2017.
- [29] K. B. MacAdam, S. F. Dyubko, V. A. Efremov, A. S. Kutsenko, and N. L. Pogrebnyak, *J. Phys. B: At., Mol. Opt. Phys.* **45**, 215002 (2012).
- [30] M. Génévriez, D. Wehrli, J. A. Agner, and F. Merkt, *Int. J. Mass Spectrom.* **435**, 209 (2019).
- [31] D. Wehrli, M. Génévriez, and F. Merkt, *Phys. Rev. A* **100**, 012515 (2019).
- [32] P. G. Burke, *R-Matrix Theory of Atomic Collisions*, Springer Series on Atomic, Optical, and Plasma Physics Vol. 61 (Springer, Berlin, 2011).
- [33] M. J. Seaton, *Rep. Prog. Phys.* **46**, 167 (1983).
- [34] W. P. Reinhardt, *Annu. Rev. Phys. Chem.* **33**, 223 (1982).
- [35] Y. K. Ho, *Phys. Rep.* **99**, 1 (1983).
- [36] E. Luc-Koenig, A. Lyras, J.-M. Lecomte, and M. Aymar, *J. Phys. B: At., Mol. Opt. Phys.* **30**, 5213 (1997).
- [37] K. Bockasten, *Phys. Rev.* **102**, 729 (1956).
- [38] E. U. Condon and G. H. Shortley, *The Theory of Atomic Spectra* (Cambridge University Press, Cambridge, 1953).
- [39] R. D. Cowan, *The Theory of Atomic Structure and Spectra* (University of California Press, Berkeley, 1981).
- [40] T. N. Rescigno and C. W. McCurdy, *Phys. Rev. A* **62**, 032706 (2000).
- [41] A. Scrinzi and N. Elander, *J. Chem. Phys.* **98**, 3866 (1993).
- [42] D. Manolopoulos and R. Wyatt, *Chem. Phys. Lett.* **152**, 23 (1988).
- [43] E. Persson, S. Yoshida, X.-M. Tong, C. O. Reinhold, and J. Burgdörfer, *Phys. Rev. A* **68**, 063406 (2003).
- [44] A. R. Edmonds, *Angular Momentum in Quantum Mechanics*, 2nd ed. (Princeton Academic Press, Princeton, 1960).
- [45] H. Bachau, E. Cormier, P. Decleva, J. E. Hansen, and F. Martín, *Rep. Prog. Phys.* **64**, 1815 (2001).
- [46] C. W. McCurdy, M. Baertschy, and T. N. Rescigno, *J. Phys. B: At., Mol. Opt. Phys.* **37**, R137 (2004).
- [47] B. Simon, *Phys. Lett. A* **71**, 211 (1979).
- [48] A. Buchleitner, B. Grémaud, and D. Delande, *J. Phys. B: At., Mol. Opt. Phys.* **27**, 2663 (1994).
- [49] T. Amemiya, Y. Kobune, H. Ito, S. Kato, K. Kitano, Y. Mizugai, and H. Maeda, *Spectrochim. Acta B* **136**, 45 (2017).
- [50] See Supplemental Material at <http://link.aps.org/supplemental/10.1103/PhysRevA.100.032517> for a detailed comparison between available data and the present theoretical results.
- [51] T. N. Rescigno and V. McKoy, *Phys. Rev. A* **12**, 522 (1975).
- [52] S. A. Bhatti, C. L. Cromer, and W. E. Cooke, *Phys. Rev. A* **24**, 161 (1981).
- [53] W. E. Cooke and C. L. Cromer, *Phys. Rev. A* **32**, 2725 (1985).
- [54] D.-S. Kim and S. S. Tayal, *J. Phys. B: At., Mol. Opt. Phys.* **33**, 3235 (2000).
- [55] E. Y. Xu, Y. Zhu, O. C. Mullins, and T. F. Gallagher, *Phys. Rev. A* **35**, 1138 (1987).
- [56] F. Gounand, T. F. Gallagher, W. Sandner, K. A. Safinya, and R. Kachru, *Phys. Rev. A* **27**, 1925 (1983).
- [57] H. Hieronymus, M. Kohl, J. Neukammer, A. König, H. Rinneberg, and H. Spinger-Bolk, *Phys. Rev. A* **41**, 1477 (1990).
- [58] E. A. J. M. Bente and W. Hogervorst, *J. Phys. B: At., Mol. Opt. Phys.* **23**, 1403 (1990).
- [59] J. G. Story, L. D. Van Woerkom, and W. E. Cooke, *Phys. Rev. A* **34**, 4508 (1986).
- [60] H. N. Ereifej and J. G. Story, *Phys. Rev. A* **60**, 3947 (1999).
- [61] F. Merkt and T. P. Softley, *Phys. Rev. A* **46**, 302 (1992).
- [62] V. L. Sukhorukov, I. D. Petrov, M. Schäfer, F. Merkt, M.-W. Ruf, and H. Hotop, *J. Phys. B: At., Mol. Opt. Phys.* **45**, 092001 (2012).
- [63] F. Merkt, *J. Chem. Phys.* **100**, 2623 (1994).
- [64] V. L. Sukhorukov, B. M. Lagutin, I. D. Petrov, H. Schmoranzler, A. Ehresmann, and K.-H. Schartner, *J. Phys. B: At., Mol. Opt. Phys.* **27**, 241 (1994).
- [65] M. Aymar, *J. Phys. B: At. Mol. Phys.* **20**, 6507 (1987).